Journal of Geophysical Research: Oceans

RESEARCH ARTICLE
10.1029/2018JC013858

Ocean Surface Layer Response to Convectively Coupled Kelvin Waves in the Eastern Equatorial Indian Ocean

Kandaga Pujiana[1,2] **and Michael J. McPhaden**[1]

[1]NOAA Pacific Marine Environmental Laboratory, Seattle, WA, USA, [2]Bandung Institute of Technology, Bandung, Indonesia

Key Points:
- Vertical heat divergence dictates surface layer thermal response to convectively coupled Kelvin waves
- Diurnal cycles in subsurface stratification and mixing are reduced in the active phase
- Barrier layer controls temporal evolution in the vertical divergence of subsurface turbulent heat flux

Correspondence to:
K. Pujiana,
kandaga.pujiana@noaa.gov

Citation:
Pujiana, K., & McPhaden, M. J. (2018). Ocean surface layer response to convectively coupled Kelvin waves in the eastern equatorial Indian Ocean. *Journal of Geophysical Research: Oceans*, *123*, 5727–5741. https://doi.org/10.1029/2018JC013858

Received 1 FEB 2018
Accepted 14 JUN 2018
Accepted article online 26 JUN 2018
Published online 18 AUG 2018

Abstract Moored measurements between June 2011 and April 2012 at 0°, 90°E in the Indian Ocean are analyzed to assess the surface layer response to the passage of 15 convectively coupled Kelvin waves. During the suppressed phase of the Kelvin waves, intense downward net surface heat flux, weak winds, and a strong diurnal cycle were evident. The net surface heat flux was 3 times larger than turbulent cooling at the base of the surface layer, accounting for an increase of surface layer temperature by +0.2 °C on average. In contrast, strong winds, heavy rainfall, diminished diurnal variations, and air-sea heat loss marked the active phase, during which surface layer cooling from above by air-sea fluxes and from below by subsurface turbulent mixing led to a decrease in surface layer temperature by −0.3 °C. Strong salinity stratification formed a thick barrier layer during the active phase, inhibiting the downward diffusion of heat below the surface layer.

1. Introduction

Precipitation within the tropics is organized over a broad range of spatial and temporal scales, from mesoscale convective systems that persist for several hours to the Madden-Julian Oscillation (MJO) at 30- to 90-day time scales (Kiladis et al., 2009). At intermediary scales between 3 and 20 days, convectively coupled Kelvin waves (hereafter referred to Kelvin waves) predominantly dictate tropical rainfall variability (Kiladis et al., 2009). Kelvin waves are typically driven by evaporation wind feedback and exhibit horizontal scales of 3,300–6,600 km (Ridout & Flatau, 2011). They propagate eastward along the equator at phase speeds of 12–20 m/s, which are faster than the MJO phase speeds of 4–5 m/s. Although the extent to which Kelvin waves might modulate the MJO remains unknown, the close connection between the waves and the MJO is well documented. Kelvin waves along with zonally migrating, synoptic equatorial waves form a substructure of organized cloudiness within the larger convective envelope of the MJO (Roundy, 2008). Together with the MJO, Kelvin waves interact with a wide range of various tropical weather systems from the onset of the winter monsoon over Indonesia and summer monsoon over the South China Sea (Straub et al., 2006; Wheeler & McBride, 2005) to the genesis of tropical cyclones (Ventrice et al., 2012).

Air-sea interactions are an important component in the initiation and propagation of Kelvin waves. Preconditioning of the atmosphere by shallow convection, sensitive to sea surface temperature (SST), controls the initiation of Kelvin waves (Seo et al., 2012). A narrow meridional structure of SST along the equator appears to set a favorable condition for the formation of Kelvin waves (Kang et al., 2013). How SST-controlled surface heat fluxes modulate the Kelvin waves, however, is not yet clear and requires a better understanding on how the upper ocean responds to the Kelvin waves.

While fundamental atmospheric structures of atmospheric Kelvin waves are relatively well documented, recent literature on the upper ocean's response to the waves is rather limited, particularly in the eastern Indian Ocean. Employing Seaglider-derived data between 20 November and 1 December 2011 at 0°, 80°E in the central Indian Ocean, Baranowski et al. (2016) reported the response of the upper ocean to two consecutive Kelvin waves, which primarily suppressed the diurnal cycle in SST and resulted in a decrease of bulk SST of 0.1 °C. They further argued that these SST responses were important to the MJO cycle. Nevertheless, it is not yet clear whether surface fluxes were the only component governing the SST responses to the Kelvin waves, or if oceanic process contributed too.

Here we aim to elucidate impacts of convectively Kelvin waves on upper ocean processes at 0°, 90°E in the eastern equatorial Indian Ocean, where SST and outgoing longwave radiation (OLR) exhibit active variations

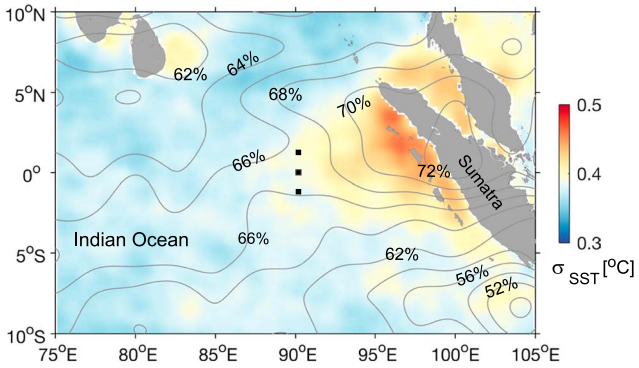

Figure 1. Standard deviation of sea surface temperature (SST) variations in the 3- to 20-day periods in the central-eastern Indian Ocean. Contours indicate percentage of outgoing longwave radiation (OLR) variations at period 3–90 days accounted for by 3- to 20-day period fluctuations. Black rectangles show Research Moored Array for African-Asian-Australian Monsoon Analysis and Prediction moorings along 90°E. The SST and OLR are satellite-derived data observed between 1998 and 2012.

on time scales of the Kelvin waves (Figure 1). Specifically, we will focus on identifying the general characteristics of the impacts and quantifying the relative contributions of air-sea exchanges and oceanic processes to the upper ocean's thermal response. Using a set of moored observations that includes direct subsurface mixing measurements over the course of June 2011 to April 2012, we posit that air-sea heat fluxes and oceanic processes together dictate the thermal response of the upper ocean to convectively coupled Kelvin waves in the eastern equatorial Indian Ocean.

The rest of this paper starts with section 2 describing the data sets and methodology used to identify Kelvin waves. Section 3 illustrates general features of the Kelvin waves in the data sets. An examination of the heat budget in the upper ocean to assess the role of surface forcing and oceanic processes in governing the upper ocean's thermal response to the Kelvin waves is discussed in section 4. A summary and discussion follow.

2. Data and Methods

2.1. Moored, Satellite Retrieved, and Reanalysis Data

The main data presented here are 3-hr averages of surface and subsurface data observed during June 2011 to April 2012 from a surface mooring at 0°, 90°E in the eastern Indian Ocean (Figure 1) deployed as part of the Research Moored Array for African-Asian-Australian Monsoon Analysis and Prediction (RAMA, McPhaden et al., 2009). Surface data consist of meteorological parameters including wind velocities, air temperature, relative humidity, rainfall rate, and shortwave radiation, while subsurface data consist of temperature (T), salinity (S), zonal (u), and meridional (v) current velocities, and turbulent microstructure measurements that relate to vertical mixing. Surface wind stress (τ) and air-sea heat fluxes are estimated using the COARE bulk formula defined in Fairall et al. (2003) with moored surface data given as inputs. Time series of the total surface heat flux (J_q^0), rainfall, and wind stresses are shown in Figures 2a–2c. Note that J_q^0 is the sum of shortwave, longwave, latent, and sensible heat fluxes.

Within the upper 100 m, T measurements were recorded at 1, 10, 13, 20, 40, 60, 80, and 100 m, while S measurements were made at 1, 10, 40, 60, and 100 m (Figures 2e and 2f). Observed T and S at 1-m are nominally designated SST and sea surface salinity, respectively (Figure 2d). SST data from RAMA moorings at 1.5°N, 90°E and 1.5°S, 90°E (Figure 1) are also analyzed to provide insights into the meridional structure of the ocean's response to Kelvin waves along 90°E.

The upper ocean currents data are from a point current meter, deployed at 10 m on the surface mooring and from an Acoustic Doppler Current Profiler (ADCP) deployed on a subsurface mooring about 4 km away from the surface mooring. The ADCP measured current profiles at depths between 30 and 1,120 m with 10-m vertical resolution. Velocities between the surface and the top most depth resolved by the ADCP are linearly extrapolated from the ADCP velocities at 40 m. The linearly extrapolated velocities are statistically comparable with the current meter velocities at 10 m, with a correlation (r) of 0.86 for u and 0.65 for v (p values < 0.001). Other studies employed a similar method to estimate near-surface velocities unresolved by the ADCP

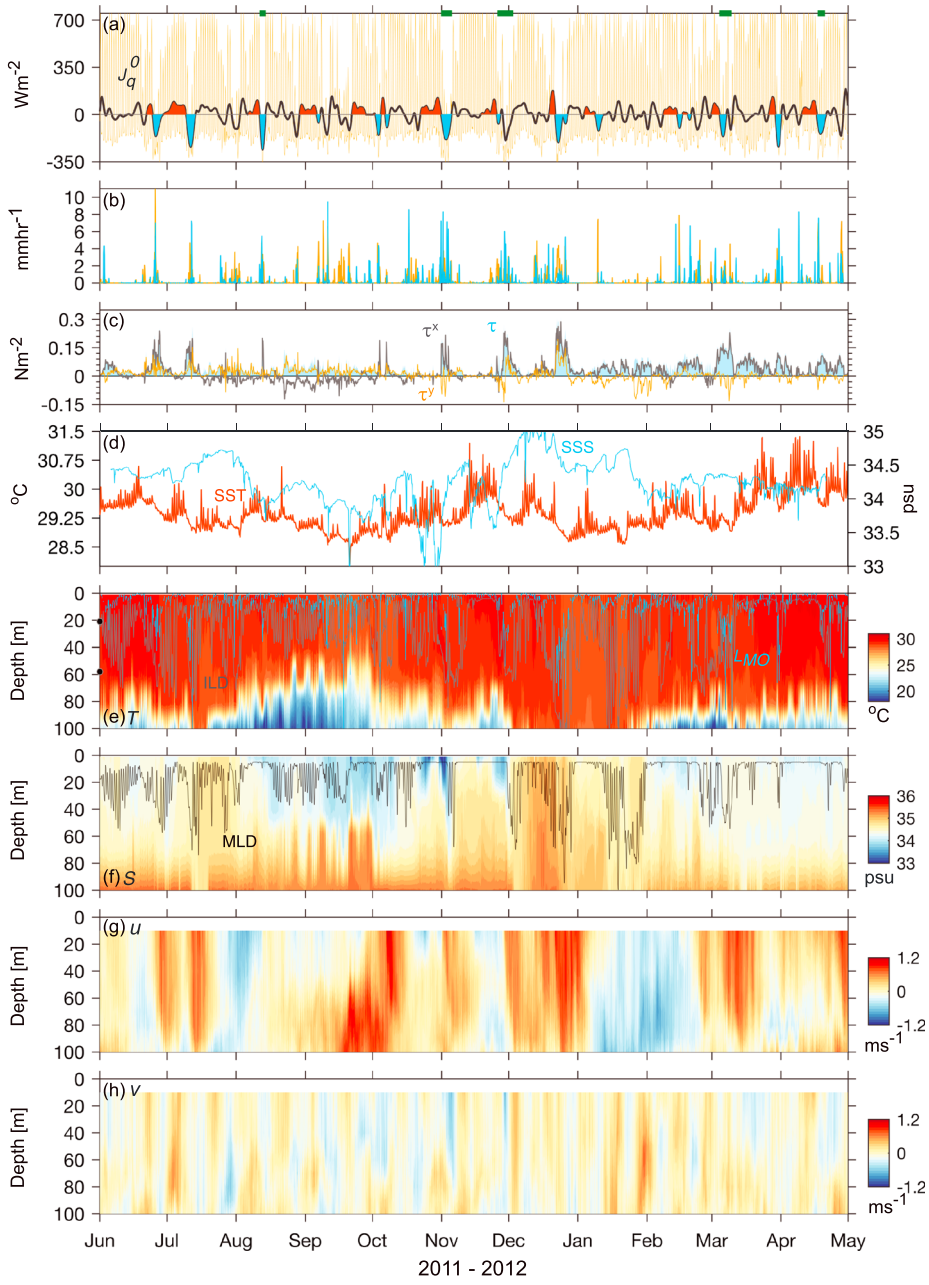

Figure 2. Time series of 3-hr averages of (a) J_q^0, (b) rainfall rate, (c) τ (blue), zonal wind stress τ^x (gray), and meridional wind stress τ^y (orange), (d) sea surface temperature (SST; red) and sea surface salinity (SSS; blue), (e) T, (f) S, (g) u, and (h) v at the 0°, 90°E mooring observed through June 2011 to April 2012. Thick black curve on (a) indicates 3- to 20-day band-pass filtered J_q^0. Positive J_q^0 values indicate surface warming. Shaded red and blue areas on (a) respectively mark the suppressed and active phases, as defined in the text. Green bars on (a) denote active phases of the Madden-Julian Oscillation (MJO). The real-time multivariate MJO (RMM) index derived by Wheeler and Hendon (2004) is used to determine the active phases of the MJO. An active phase of the MJO is defined when RMM index > 1. Rainfall rate was observed by the rain gauge (blue) and by Tropical Rainfall Measuring Mission satellite (orange). Positive τ^x (τ^y) values denote eastward (northward) wind stress. Positive u (v) values denote eastward (northward) current. Gray and blue curves on (e) and black curve on (f) respectively indicate the isothermal layer depth (ILD), Monin-Obukhov length (L_{MO}), and mixed layer depth (MLD), as defined in the text. Black dots on the y axis of (e) mark the χpod depths.

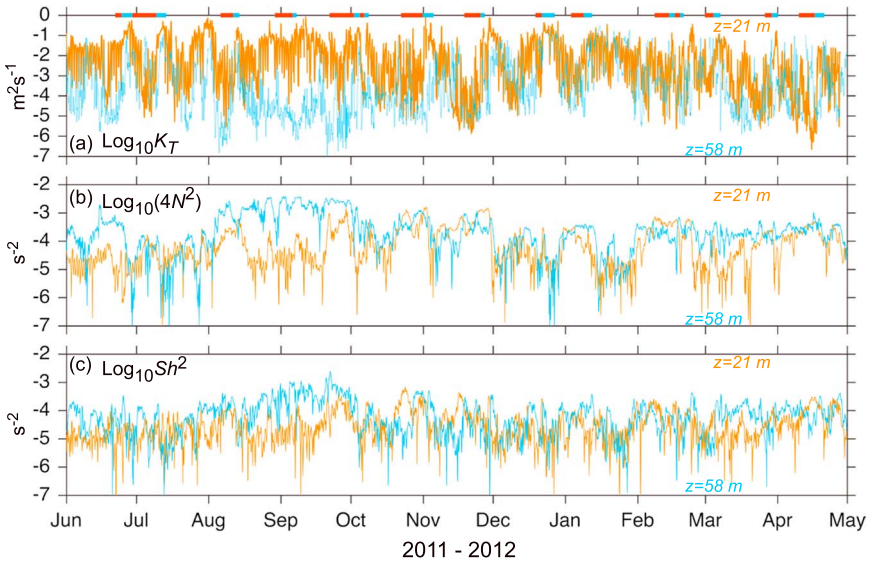

Figure 3. Time series of 3-hr averages ($\log_{10}$) of (a) K_T, (b) $4{\times}N^2$, and squared vertical shear Sh^2 at 21 m or surface layer base (orange) and 58 m (blue) observed at the 0°, 90°E mooring during June 2011 to April 2012. Red and blue bars on (a) mark the suppressed and active phases of the Kelvin waves.

in the central equatorial Indian Ocean (Nagura & McPhaden, 2010). The velocities in the upper 100 m are illustrated in Figures 2g and 2h.

Microstructure data are from χpods, that is, moored fast response thermistors, which were deployed at 21 and 58 m. T was sampled at 10 Hz and its analog time derivative (T_t) at 120 Hz. Measured T_t permits calculations of variance dissipation rate (χ_T) and the turbulent kinetic energy dissipation (ϵ_χ) using procedures documented in Moum and Nash (2009). We then estimate the turbulent thermal diffusivity, $K_T = \Gamma\epsilon_\chi/N^2$ (Figure 3a), and turbulent heat flux , $J_q = -\rho C_p K_T \partial T/\partial z$ at the χpod depths, where Γ is mixing efficiency, N^2 is squared Brunt-Väisälä frequency (Figure 3b), ρCp is the volumetric heat capacity, and $\partial T/\partial z$ is vertical derivative of temperature. The Γ value is specified as 0.2 (Osborn, 1980).

In addition to the moored data, satellite data and atmospheric reanalysis outputs are also examined. The satellite data are gridded outgoing OLR, rainfall rate, surface wind velocities, and SST. The gridded OLR (Liebmann & Smith, 1996), precipitation, and wind data have spatial and temporal resolutions of 0.25° × 0.25° and 3 hr. Rainfall is obtained from the Tropical Rainfall Measuring Mission (TRMM) Microwave Imager satellite products, and surface wind is from a multisensor and blended product (Bentamy & Fillon, 2012). The satellite-retrieved wind data are utilized to fill a gap in the moored wind time series between 18 January and 30 April 2012 as both satellite-derived and moored wind data show a good agreement between 1 June 2011 and 17 January 2012 ($r = 0.84$ and $p < 0.001$). The SST data are from the Gridded High-Resolution SST product with daily temporal resolution and spatial horizontal resolution of 0.01°× 0.01° (Donlon et al., 2009).

2.2. Kelvin Wave Identification

The convective Kelvin wave events at 0°, 90°E are identified using two procedures. First the gridded TRMM rainfall data are averaged at a latitude domain from 5°N to 5°S and then filtered using the Wheeler wavenumber-frequency filter (Wheeler & Kiladis, 1999) to form a set of two-dimensional (wavenumber-frequency) Fourier filtered satellite-retrieved precipitation data. The wavenumber-frequency data are then subsampled to isolate rainfall variability with wavenumbers (1 to 14) and frequencies (1/20 and 0.4 cycles per day), typical of atmospheric Kelvin waves. The retained rainfall data in the wavenumber-frequency domain are subsequently transformed back to the longitude-time domain (hereafter the filtered rainfall data).

The second procedure compares the filtered satellite-retrieved rainfall data with the moored rainfall data at 0°, 90°E. Only Kelvin wave events that have a detectable rainfall rate >0.5 mm/hr for over a period of at least a full day (daytime and nighttime rain) both in the satellite-derived and moored data are considered for the present analysis. Using the aforementioned criteria, we identified 15 Kelvin wave events at the 0°,

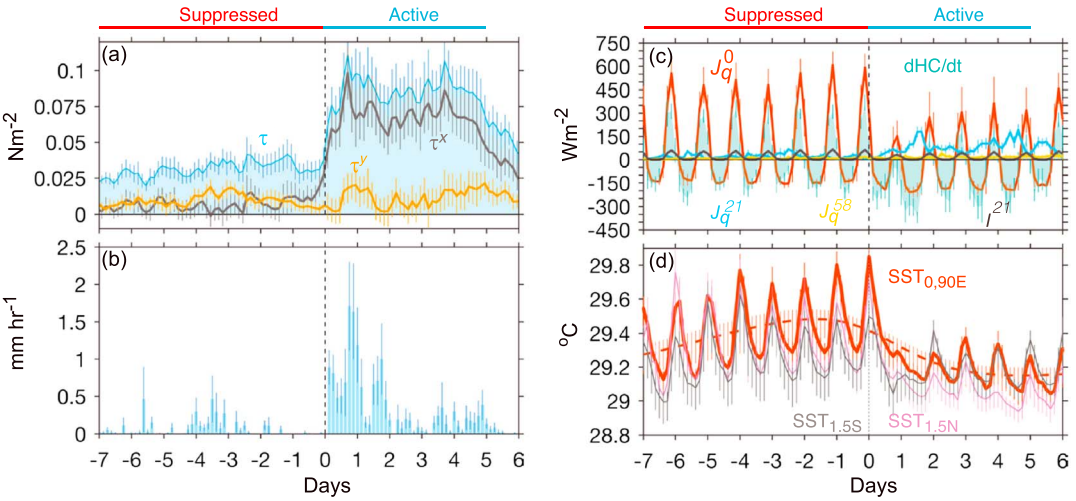

Figure 4. Composite averaged time series of surface and subsurface data at the 0°, 90°E mooring for the 15 Kelvin wave events observed over the course of June 2011 to April 2012. (a) τ (blue), τ^x (black), τ^y (orange). (b) Rainfall rate. (c) Surface layer heat content (HC) tendency $\rho C_p h \partial \overline{T}/\partial t$, and surface and subsurface turbulent heat fluxes. $\overline{T}$ is the vertically integrated temperature between the surface and the base of the surface layer $h = 21$ m. J_q^0 (red), fraction of shortwave radiation penetrating the surface layer base I^{21} (black), HC tendency (green), J_q^{21} (blue), and turbulent heat flux at 58 m J_q^{58} (gold). Positive J_q^0 values indicate that the total surface heat flux warms the surface. Positive J_q^h values indicate downward subsurface turbulent cooling at a fixed depth of h, with positive values implying cooling of the surface layer. (d) Sea surface temperature (red) and its low-pass (3 days) filtered time series (red dashed line). Purple and gray curves show sea surface temperature at 1.5N°, 90°E, and 1.5S°, 90°E, respectively. Color coded thin vertical lines denote 95% bootstrap confidence limits.

90°E mooring over the course of June 2011 to April 2012 (shaded J_q^0 in Figure 2a). Each passage was composed of preconvective (hereafter referred to as a suppressed) phase and a convective (hereafter active) phase. The suppressed Kelvin wave phase is defined by band-pass (3- to 20-day periods)-filtered total surface heat flux $J_q^0 > 0$ W/m^2 and $\tau < 0.05$ N m^2, while the active phase is defined by band-passed filtered $J_q^0 < 0$ W/m^2 and $\tau^x > 0.05$ N/m^2 (Figures 2a and 2c). The surface-moored measurements indicate that the suppressed and active phases spanned, on average, 7 and 5 days, respectively. In the present analysis, we consider only those Kelvin waves with the suppressed and active phases longer than 2 days.

3. Surface and Subsurface Responses

To evaluate the general characteristics of the upper ocean's response to the suppressed and active phases of the Kelvin waves, composite averaged time series of the surface and subsurface data over the course of the Kelvin wave phases are determined. The composite time series is obtained by averaging the surface and subsurface time series attributed to the 15 Kelvin wave events from 7 days prior to the active phase onset to 6 days after the onset, so that the averaged time series sufficiently resolves the average cycle of a Kelvin wave. The onset time (day = 0) is arbitrarily referenced to warmest daytime SST at the end of the suppressed phase.

3.1. Suppressed Phase

Sea surface signatures of the suppressed phase were marked by weak wind stress, little rain, intense surface heating, and active diurnal variations. τ varied around 0.03 N/m^2, while average precipitation rate was roughly 0.24 mm/hr (Figures 4a and 4b). Excess daytime J_q^0-induced warming over nighttime J_q^0-induced cooling likely accounted for an overall SST increase over the course of the suppressed phase (red curves in Figures 4c and 4d), during which the average magnitude of the SST changes (δSST) on the Kelvin wave time scales increased by 0.2 °C (Figure 5a). For each Kelvin wave event, δSST is defined as the difference between maximum and minimum of low-pass (3 days) filtered SST observed through the suppressed phase.

Like in J_q^0, diurnal variations were also evident in SST as well as stratification and subsurface mixing in the upper 21 m (hereafter arbitrarily defined as the surface layer) during the suppressed phase. The diurnal SST amplitudes (δSST_d), obtained by subtracting the SST value at local sunrise time from the daytime SST maximum on the same day, were large with a mean of 0.45 °C (Figure 5b). Diurnal SST variations appeared to modulate the SST warming through the suppressed phase as the average δSST_d values exhibited a significant positive

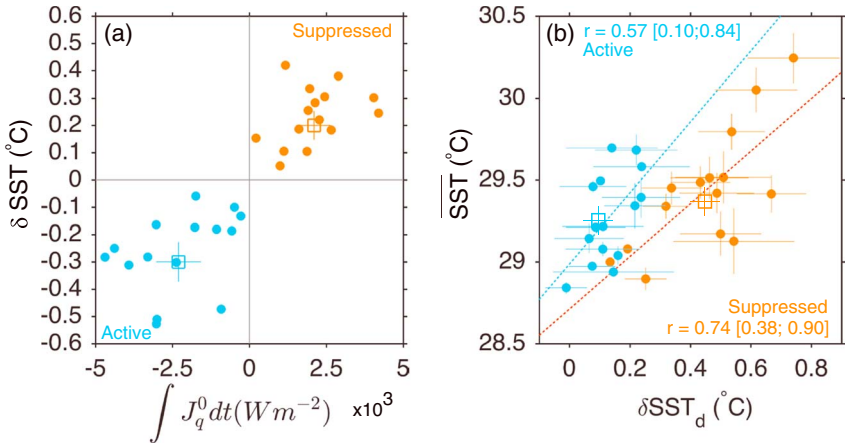

Figure 5. (a) Accumulated J_q^0 versus δSST and (b) δSST_d versus mean sea surface temperature (SST) during the suppressed phase (orange) and the active phase (blue) observed at 0°, 90°E during June 2011 to April 2012. Each color-coded data point shown in (a) and (b) is an average during each respective phase of the 15 Kelvin wave events. Values in brackets in (b) represent 95% confidence limits. Dashed lines in (b) indicate the least squares lines. Color-coded rectangles and lines respectively indicate average values and 95% bootstrap confidence limits.

correlation with the mean SST values ($r = 0.74$, $p < 0.001$; orange circles in Figure 5b). A similar relationship between δSST_d and daily SST mean was observed at the central equatorial Indian Ocean (Seo et al., 2014).

The off equatorial moorings exhibited a similar SST response to the suppressed phase, with the SST increasing by 0.2 °C (Figure 4d). Satellite-retrieved SST demonstrate that SST warming during the suppressed phase extended zonally between 80°E and 100°E, with the largest warming observed at the equator off Sumatra island (Figure 6a). Deep thermocline and river runoff off Sumatra might facilitate a stronger coupling between J_q^0 and SST, explaining pronounced SST warming during the suppressed phase observed in this region. In the north-south direction, the SST response is roughly symmetric about the equator.

N^2 at the base of the surface layer was mainly controlled by salinity, peaked in the afternoon and subsequently decayed during nighttime (Figure 7a). K_T attained its average maximum magnitude of 2×10^{-2} m^2/s at around dawn, an order of magnitude larger than its minima registered in the afternoon (Figure 7c). On longer time scales neither N^2 nor K_T at the base of the surface layer exhibited a noticeable trend over the suppressed phase, and N^2 was salinity controlled (Figures 7a and 7c). Beneath the surface layer, daily K_T peaks were less pronounced (Figure 7d). This likely relates to more stratified subsurface layer (Figure 7b) or is linked to the shallow surface mixed layer. The mixed layer depth (MLD), defined as a density increase of 0.01 kg/m^3 above the surface value, varied between 10 and 15 m during the suppressed phase (Figure 8a).

Recurring nighttime K_T peaks corresponded with downward turbulent heat flux at the base of the surface layer ($J_q^{21}>0$; blue curves in Figures 4c and 7c), diffusing heat from the surface layer to deeper depths at an average magnitude of 15 W/m^2 during the suppressed phase. This nighttime turbulent cooling across the surface layer base was more likely due to subsurface convection than shear instability. The mean absolute value of Monin-Obukhbov length, $|L_{MO}| = |-\frac{\tau^0}{\rho}/\kappa J_b^0|$, a parameter used to indicate the depth where buoyant destruction of turbulence and shear production of turbulence are equally important or of the same order, where κ is von Karman's constant and J_b^0 is buoyancy flux, was about a fourth of the average MLD measured through the suppressed phase (Figure 8a). Since $|L_{MO}|$ was smaller than the average MLD, buoyancy destruction was more dominant than shear production to account for elevated nighttime turbulence within the surface layer. Moreover, gradient Richardson number ($Ri = N^2/Sh^2$), in which Sh^2 is squared shear ($Sh^2 = \frac{\partial u^2}{\partial z} + \frac{\partial v^2}{\partial z}$), was predominantly larger than 0.25 at the surface layer base during the suppressed phase (Figure 9). Although strongest Sh^2 approximately occurred in phase with strongest N^2 during the day (Figures 7a and 7c), it was not strong enough to destabilize the stratification and to cause daytime surface layer turbulence. Emphasized by both small $|L_{MO}|$ and $Ri > 0.25$, convective-driven turbulence was hence more dominant than shear instability in producing the nighttime turbulence bursts through the suppressed phase.

Aided by weak wind stresses, surface layer velocities during the suppressed phase were primarily characterized by semidiurnal and diurnal tidal currents (Figure 7e). On the Kelvin wave time scale, u and v were in

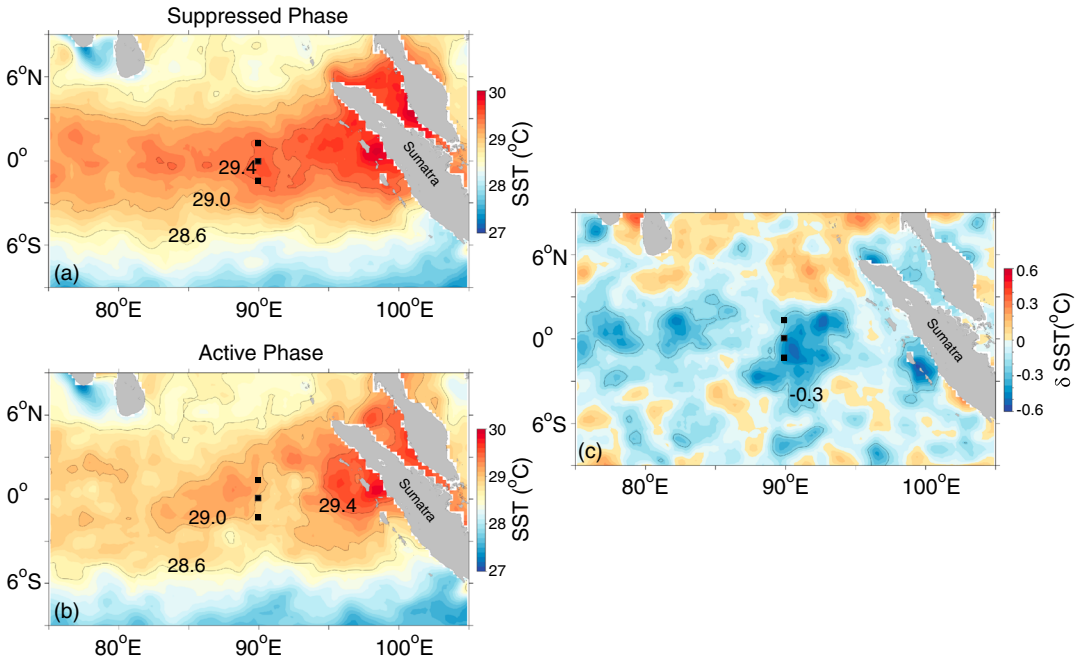

Figure 6. Composites of satellite-derived sea surface temperature (SST) for the 15 Kelvin wave events observed over the course of June 2011 to April 2012. (a) Demonstrates the composite at day = −2 during the suppressed phase, (b) shows the composite at day = +5 during the active phase, and (c) indicates (b) - (a). Black rectangles show Research Moored Array for African-Asian-Australian Monsoon Analysis and Prediction moorings along 90°E.

general indistinguishable from zero through the suppressed phase (Figure 7e). This dynamic response also extended beneath the surface layer (Figure 7f).

3.2. Active Phase

During the ensuing active phase of the Kelvin waves, wind stress and precipitation substantially increased, and there was a net cooling of the sea surface by the atmosphere. Average τ^x increased by a factor of 6, compared to that over the course of the suppressed phase, while average meridional wind stress (τ^y) did not exhibit a noticeable increase (Figure 4a). Concurrent with more energetic wind stress, upward total surface heat flux (J_q^0 <0; red curve on Figure 4c) intensified and thereby cooled SST (red curve on Figure 4d), with a mean of δSST over the active phase of −0.3 °C (Figure 5a, lower left quadrant). Here δSST for each Kelvin wave event is given as the difference between the coldest low-pass filtered SST observed during the active phase and the warmest low-pass filtered SST registered during the suppressed phase. Like during the suppressed phase, SST at the off equatorial moorings substantially declined during the active phase (Figure 4d). Satellite-derived SST indicates that the most pronounced surface cooling occurred around the mooring site and was roughly symmetric about the equator (Figures 6b and 6c). The horizontal structure of SST observed both during the suppressed and active phases appears to reflect theoretical atmospheric Kelvin wave structure (Kiladis et al., 2009).

The diurnal cycle of SST was attenuated during the active phase, during which δSST_d on average reduced to only 0.13 ° C (Figure 5b), 3–4 times smaller than during the suppressed phase. The diurnal SST cycle appeared to be completely diminished within the first 2 days of the active phase (Figure 4d) due to not only greatly reduced daytime positive J_q^0 but also intensified daytime cooling effect of J_q at the base of the surface layer (Figure 4c). Off-equator SSTs also exhibited a similar response to the convective phase of the Kelvin wave (Figure 4d).

Despite of intense surface cooling by air-sea fluxes, surface layer N^2 gradually strengthened within the first half of the active phase (Figure 7a). The gradual increase of N^2 was primarily driven by a rapid increase of salinity stratification (N_S^2), likely due to the formation of freshwater pools following heavy rainfall during the active phase, that exceeded the rate at which surface layer thermal stratification (N_T^2) was reduced by surface heat loss (Figures 7a and 8a). Surface layer N^2 then quickly declined through the remainder of the active phase, coincident with reduced rainfall (Figures 7a and 4b). Either advection of the freshwater pools away from our

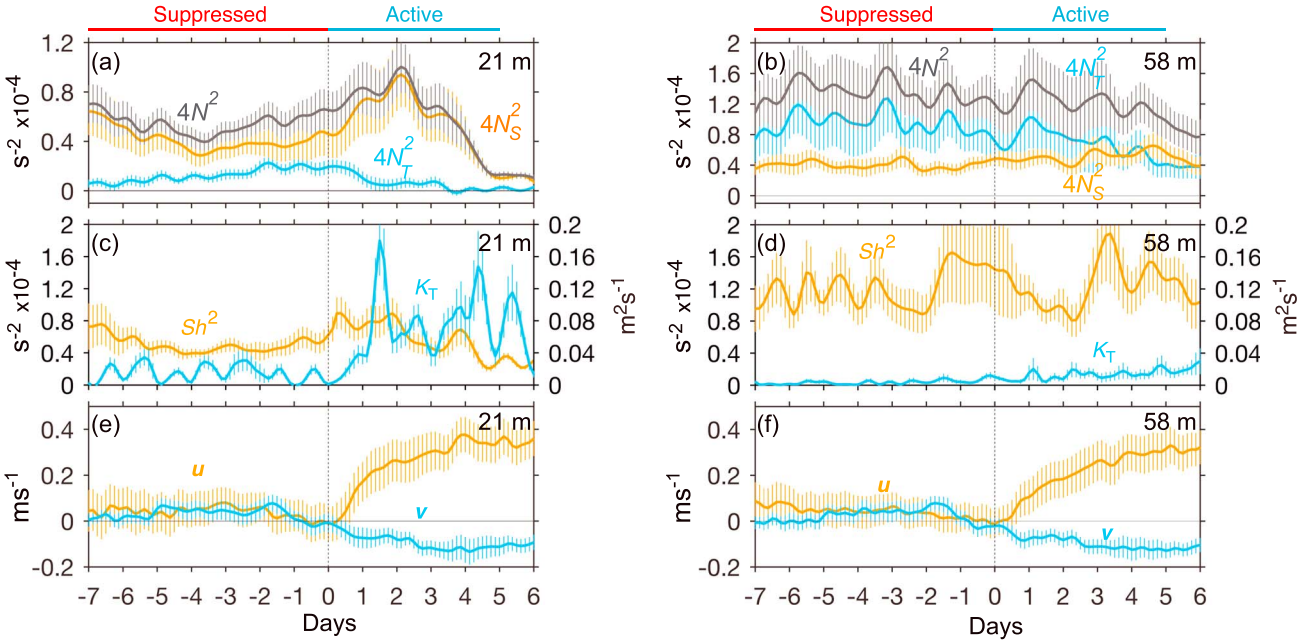

Figure 7. (a) Composite averaged time series of $4{\times}N^2$ at (a) 21 m and (b) 58 m, Sh^2, and K_T at (c) 21 m and (d) 58 m, and u and v at (e) 21 m and (f) 58 m observed at the 0°, 90°E mooring for the 15 Kelvin wave events over the course of June 2011 to April 2012. N_T^2 and N_S^2 in (a) and (b) respectively denote temperature and salinity stratifications. N_T^2 and N_S^2 are respectively expressed as $g\alpha\partial T/\partial z$ and $-g\beta\partial S/\partial z$, where g, α, and β are gravitational acceleration, the haline contraction coefficient, and the thermal expansion coefficient, respectively. Color coded thin vertical lines denote 95% bootstrap confidence limits.

station or upward diffusion of salty sea water from below the surface layer, or both, might explain the attenuation of surface layer N^2. Below the surface layer, where thermal stratification was dominant, N^2 generally weakened with time through the active phase (Figure 7b).

Subsurface turbulence was substantially enhanced during the active phase. Surface layer K_T rapidly increased to reach an average magnitude of 0.07 m^2/s over the first day of the active phase (Figure 7c), and it sustained this level of diffusivity while transferring heat downward with an average magnitude of 45 W/m^2 through the rest of the active phase (Figure 8c). At 58 m, the average downward J_q^{58} during the active phase was 17 W/m^2, almost twice as large as the average J_q^{58} during the suppressed phase (10 W/m^2; gold curve in Figure 8c). In comparison to the amount of heat diffused downward through the surface layer base during the active phase of the MJO, atmospheric Kelvin wave-induced turbulent heat flux appears smaller. Turbulence profiles at the

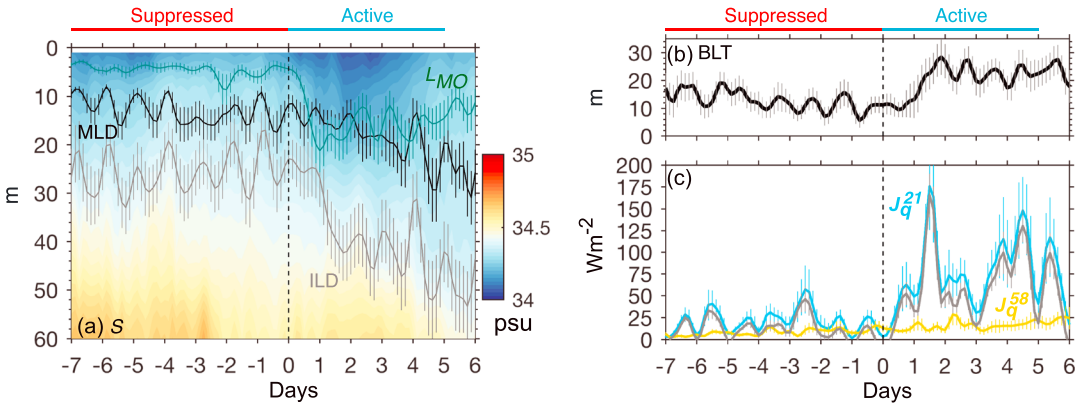

Figure 8. Composite averaged time series of (a) S (b) barrier layer thickness (BLT), and (c) J_q at the surface layer base at 21 m (blue) and 58 m (gold) observed at the 0°, 90°E mooring for the 15 Kelvin wave events over the course of June 2011 to April 2012. Contours overlaid on (a) are the composites of mixed layer depth (MLD) (black), isothermal layer depth (ILD; gray), and L_{MO} (green). Gray curve on (c) indicates turbulent heat divergence between 21 and 58 m. Color coded thin vertical lines denote 95% bootstrap confidence limits.

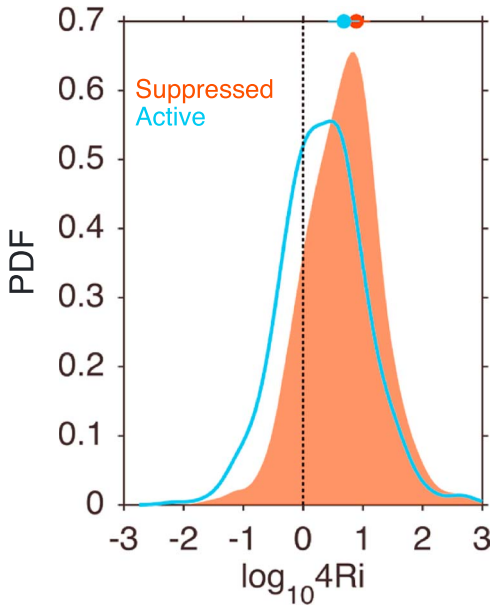

Figure 9. Distribution of nighttime ($\log_{10}$) 4Ri at the surface layer base during the suppressed phase (orange) and the active phase (blue) of the 15 Kelvin waves observed at 0°, 90°E between June 2011and April 2012. Color coded circles indicate the median values of the distribution. Vertical dashed line indicates $Ri = 1/4$.

central equatorial Indian Ocean indicate that turbulent heat flux across the MLD under a MJO convective system is on average in the order of ~100 W/m^2 (Pujiana et al., 2018).

Rapid eastward acceleration is a salient feature of the dynamic response in the surface layer to the strong westerly wind stress during the active phase, with u accelerating eastward from almost at rest to 0.45 m/s (Figure 7e). The eastward jet was also observed at 58 m but with a weaker speed (Figure 7f). In the meridional direction, the mean surface current was interestingly southward although the average τ^y was northward during the active phase (Figures 7e and 4a). Forcing other than the local winds, for example, in the form of mixed-Rossby gravity (Yanai) waves, might account for v during the active phase (Sengupta et al., 2004). Alternatively, there may be a very shallow downwind flow above 10 m that is not captured in our 10-m current record, below which the flow we do observe runs counter to the meridional winds driven by meridional pressure gradient set up by those winds.

The rapid wind-driven eastward acceleration in the surface layer, overlying a slower moving layer at greater depths, amplified vertical shear. Sh^2 at the surface layer base increased through the first few days of the active phase and decayed afterward (Figure 7c). Meanwhile, maximum shear was observed at 58 m toward the end of the active phase (Figure 7d), implying a descending sheared layer with time. This time evolution of the sheared layer depth through the active phase might reflect the role of turbulence to vertically distribute eastward momentum from the surface to deeper depths. Increased vertical shear tended to destabilize the surface layer during the active phase, consistent with more occurrences of $Ri < 0.25$ events (Figure 9). Moreover, the MLD was roughly comparable to $|L_{MO}|$ for the most part of the active phase (Figure 8a), indicating that shear instability contributed more as a source of surface turbulence during the active phase than during the suppressed phase.

The barrier layer, defined as the region between the mixed layer and the isothermal layer, seems to play a role in dictating vertical divergence of turbulent heat fluxes during the Kelvin wave phases. The barrier layer thickness (BLT) was relatively thin through the suppressed phase and increased over the active phase, in response to a rapid deepening of the isothermal layer (Figures 8a and 8b) defined as the depth over which temperature changes by an equivalent to 0.01 kg/m^3 assuming constant salinity (Figure 8a). Deepening of the isothermal layer would be expected due to Ekman convergence and downwelling driven by strong westerly winds during the active phase. Westerly winds near the equator drive southward Ekman flow north of the equator and northward Ekman flow south of the equator, leading to flow convergence and downwelling on the equator. The base of the Ekman layer near the equatorial Indian Ocean is around 40 m (Wang & McPhaden, 2017),

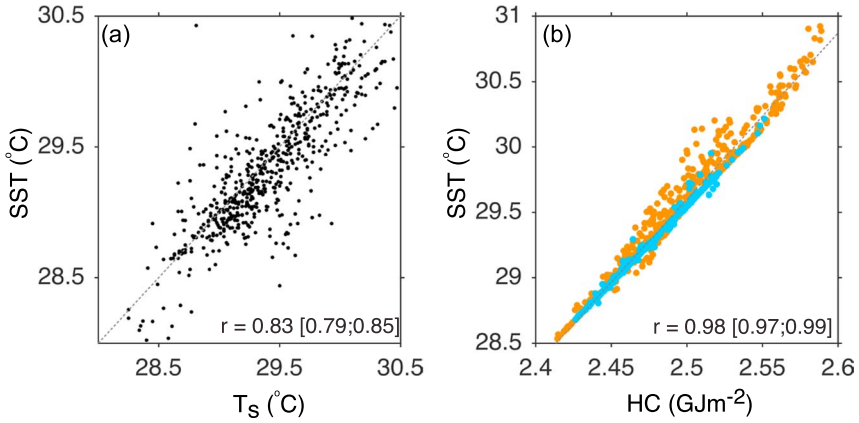

Figure 10. (a) Satellite-derived sea surface temperature (SST) (T_s) values versus daily SST averages. (b) Surface layer heat content (HC) versus SST during the suppressed phase (orange) and the active phase (blue) of the 15 Kelvin waves. The data shown in (a) and (b) were observed at 0°, 90°E between June 2011 and April 2012. Values in brackets in (a) and (b) represent 95% confidence limits.

which is the same order of magnitude of the average ILD observed during the active phase, suggesting that Ekman dynamics is playing role in determining ILD. On the other hand, heavy rainfall would tend to strengthen salinity stratification, retarding MLD deepening at the same rate as the isothermal layer depth (ILD). During the suppressed phase, the BLT varied between 10 and 15 m (Figure 8b) and the average vertical divergence between J_q^{21} and J_q^{58} was about 8 W/m^2 (Figure 8c). The BLT doubled during the active phase (Figure 8b), and the turbulent heat flux divergence increased twofold to threefold (Figure 8c), indicating that the barrier layer tended to inhibit downward turbulent heat flux with depth. However, the precise depth range over which turbulent heat flux divergence occurred cannot be determined because we had only two χpods between 21 and 58 m.

During the convective phase of the MJO, the barrier layer generally tends to be thinner than during the suppressed phase (Chi et al., 2014). Based on analysis of three MJO events over the central equatorial Indian Ocean, Chi et al. (2014) posited that enhanced vertical shear attributed to the active phase of the MJO active was sufficiently strong to counteract the barrier layer potential energy and hence erode the barrier layer. Compared to the eastern equatorial Indian Ocean, salinity stratification in the surface layer in the central part of the basin is weaker, which is a favorable condition for the MJO to erode the barrier layer.

4. Surface Layer Heat Budget

Observations reveal that surface forcing attributed to 15 atmospheric Kelvin wave pulses effected temperature, salinity, stratification, turbulence, and current variations in the surface layer at 0°, 90°E registered during June 2011 to April 2012. In this section, we further quantify the contributions of surface forcing and oceanic processes in governing the temporal evolution of the thermal response in the surface layer to those pulses. These contributions are assessed using a simplified heat equation integrated in the surface layer between the surface and a fixed depth of $h = 21$ m, given by

$$\rho C_p h \frac{\partial \overline{T}}{\partial t} = (J_q^0 - I^h - J_q^h) - \rho C_p h \left(\overline{u} \frac{\partial T_s}{\partial x} + \overline{v} \frac{\partial T_s}{\partial y} \right) + R, \quad (1)$$

where $\overline{T}$, $\overline{u}$, and $\overline{v}$ respectively are moored T, u, and v averaged across the surface layer, J_q^h is turbulent heat flux acting across the surface layer base, I^h is the fraction of shortwave heat flux penetrating below the surface layer base and determined from an empirical formulation (Ohlmann et al., 1996), T_s is satellite-derived SST, and R represents the residual term consisting of unresolved physical processes and observational errors. Zonal and meridional gradients of T_s are inferred from center differences around 0°, 90°E with a 0.25° separation. Despite its lower temporal resolution, daily samples of T_s and daily averages of moored SST at 0°, 90°E exhibit a significant correlation ($r = 0.83$ with $p < 0.001$; Figure 10a). A significant correlation is also found between T_s and $\overline{T}$ ($r = 0.78$ with $p < 0.001$), suggesting that T_s can provide a reasonable estimate of lateral SST gradients for our surface layer heat budget calculation. Changes in surface layer temperature are thus a balance

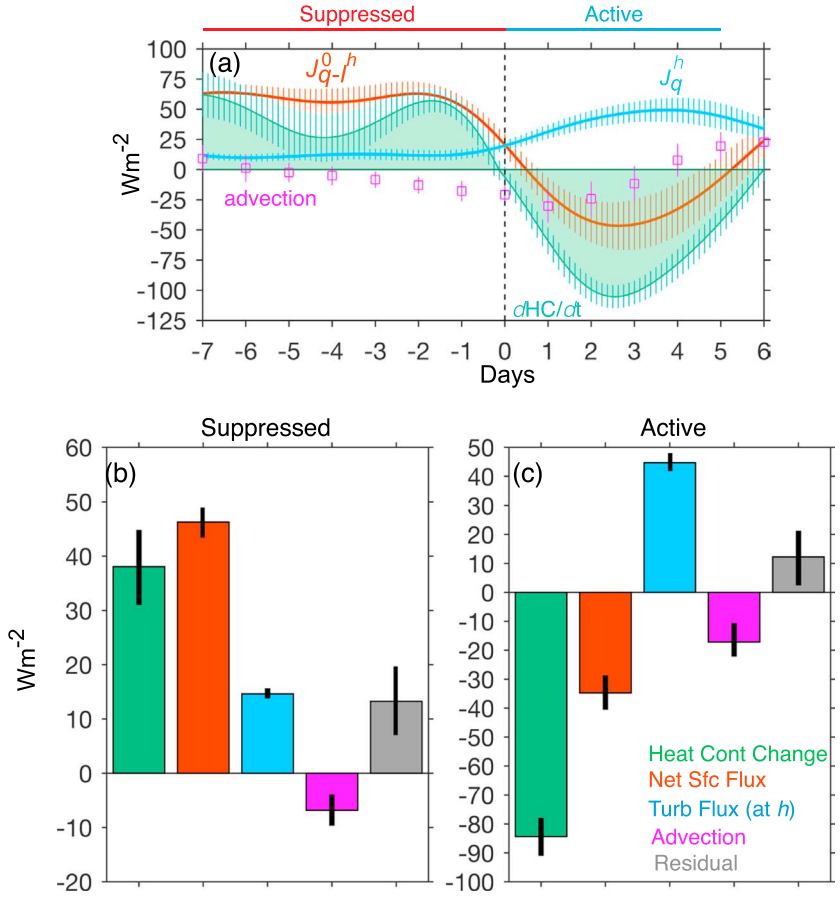

Figure 11. (a) Composite averaged time series of surface layer heat content (HC) tendency, surface and subsurface turbulent heat fluxes, and lateral advective heat fluxes in the surface layer. Average magnitudes of the heat budget terms in the surface layer during the suppressed (b) and active (c) phases of the 15 Kelvin wave events observed at 0°, 90°E between June 2011 and April 2012. Green bars indicate dHC/d*t*, red bars denote the net surface heat flux $J_q^0 - I^h$, blue bars show J_q^h (positive indicates heat loss), magenta bars denote the total advective heat fluxes $-\rho C_p h\,(\bar{u}\partial T/\partial x + \bar{v}\partial T/\partial y)$, and gray bars indicate the residual *R*. Vertical bars indicate 95% bootstrap confidence intervals.

between vertical heat flux divergence, lateral advective heat fluxes, and the residual heat flux, which includes terms in the heat balance that we cannot explicitly compute plus any computational and sampling errors in the terms that we are able to compute.

Ideally, one would want to examine the heat budget analysis in a mixed layer of variable depth. However, the wide spacing of the χpods does not allow for this. On the other hand, the heat content (HC) within the surface layer, $HC = \rho C_p \int_0^h T dz$ is significantly correlated with SST ($r = 0.98$ with $p < 0.001$; Figure 10b), so that examining the balance of terms over this fixed depth can provide insights into the processes that control SST.

Time series of each term of (1) is low-pass filtered, with a cutoff frequency of 1/3 cycle per day. Using the filtered time series, a composite of temporal evolution of the heat budget terms encompassing the suppressed and active phases of the 15 Kelvin wave pulses is then determined (Figure 11a). Based on the composite time series, averages of all terms of (1) for each phase of the Kelvin wave are subsequently computed. Note that a trapezoidal rule is employed to estimate the vertical integration of the heat budget terms.

During the suppressed phase, the surface layer was warmed from above by the net surface heat flux ($J_q^0 - I^h$) and cooled from below by turbulence (J_q^h) (Figure 11a). The vertical heat convergence, in which surface warming exceeded subsurface turbulent cooling by 31 W/m^2, accounted on average for about 80% of the surface layer warming rate (Figure 11b). We cannot, however, account for the remaining heating rate of the surface layer and balance the surface layer heat budget since advection acted to cool the layer by roughly −7 W/m^2. We suspect that our inability to close the budget is not due to neglected physical processes but rather due

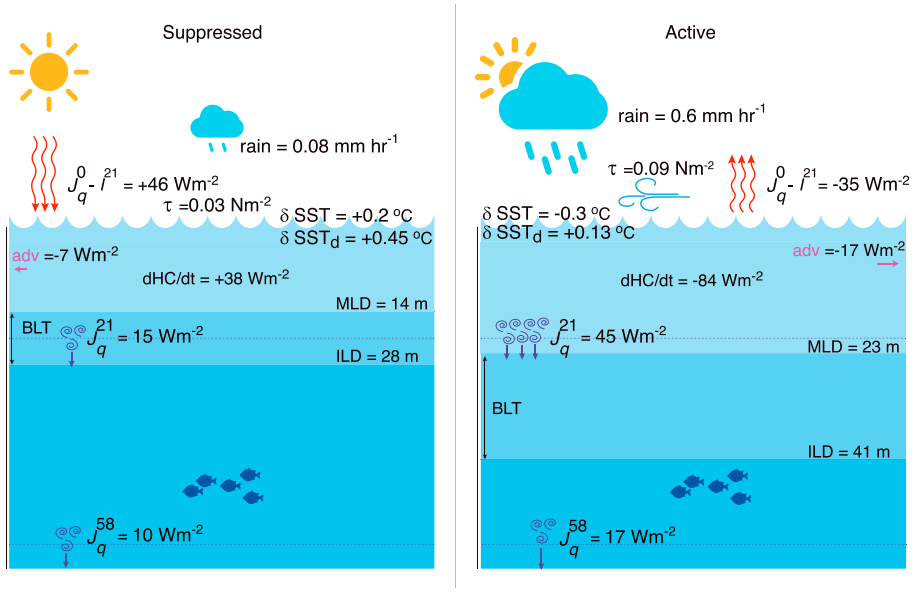

Figure 12. Schematics demonstrating the mean values of surface forcing and oceanic processes during the suppressed (left panel) and active (right panel) phases.

primarily to systematic underestimation of lateral advective heat flux. Using linearly extrapolated velocities between the surface and the topmost ADCP bin depth likely introduces errors in our velocity estimates which in turn adds uncertainty to our calculation of the lateral advective heat flux. Other possible sources of uncertainty, which would appear in the residual, include errors in our estimates of horizontal gradients of mixed layer temperature using purely surface estimates from satellites and errors in surface flux estimates based on bulk formulae. The 4-km displacement of the ADCP mooring from the surface mooring may also to introduce uncertainties in our ability to close the heat budget.

Despite this significant residual heat flux, our observations reveal that surface layer temperature heating during the suppressed phase was primarily controlled by downward total surface heat flux and turbulent mixing diffusing heat into greater depths. Thus, the average SST increase of 0.2 °C observed during the suppressed phase of the 15 Kelvin waves was predominantly driven by the vertical heat divergence, in which $(J_q^0 - I^h)/J_q^h$ was about 3, that is, the net surface heat flux was the primary driver of the surface layer warming during the suppressed phase of the Kelvin waves.

During the active phase, the net cooling of the surface layer was attributable to surface heat loss, entrainment cooling, and advection. $J_q^0 - I^h$ changed sign, while J_q^h substantially increased due to intensified subsurface convection and shear instability (Figure 11a). J_q^h continued to cool the surface layer at a smaller rate even after $J_q^0 - I^h$ resumed to warm the layer (Figure 11a). The surface and subsurface turbulent heat fluxes together explained about 95% of the surface layer cooling, while enhanced advective cooling accounted for the rest of the surface layer heat loss (Figure 11c). Unlike during the suppressed phase, the average magnitudes of $J_q^0 - I^h$ and J_q^h were roughly equal during the active phase. Surface cooling from above and subsurface turbulent cooling from below were thus equally important to explain the average SST cooling of −0.3° measured during the active phase of the 15 Kelvin waves. The residual flux, although relatively small, was significant and likely due to similar error sources as in the suppressed phase. The average magnitudes of observed surface and subsurface data during the suppressed and active phases of the Kelvin waves are summarized in Figure 12.

5. Summary and Discussion

The primary thermal response of the ocean surface layer to surface forcing attributable to the 15 Kelvin wave pulses observed at the 0°, 90°E RAMA mooring between June 2011 and April 2012 in the eastern equatorial Indian Ocean is elucidated from a suite of moored atmospheric boundary layer and upper ocean measurements, including direct ocean mixing observations. Based on our observations, the thermal response and the relative contribution of surface forcing and ocean processes to dictate the response evolve with phases of the Kelvin waves as follows.

1. During the suppressed phase, the excess of net surface heat flux over subsurface turbulent cooling is the main driver of the surface layer temperature warming. SST increases by +0.2 °C, and large diurnal SST amplitudes exhibit a significant correlation with the increasing trend of the mean SST. Sustained by weak wind stress, diurnal cycles in stratification and subsurface mixing are also evident, exhibiting daytime stratification maxima and nighttime subsurface mixing peaks, respectively. Subsurface convection is the predominant source of the nighttime mixing maxima.
2. Over the course of the ensuing active phase, air-sea heat fluxes, subsurface turbulence, and advection together dictate the surface layer temperature cooling. SST decreases by about −0.3 °C, and diurnal variations in stratification and mixing are greatly attenuated. Under intense surface cooling and strong winds, the surface layer rapidly accelerates eastward with increased turbulent cooling by 3–4 times that observed during the suppressed phase. Salinity-controlled stratification initially strengthens and then decays toward the end of the active phase. Both convection and shear instability control the turbulent cooling because $Ri < 0.25$ occurs more frequently and the MLD is comparable to the $|L_{MO}|$. A thick barrier layer, formed due to heavy precipitation-induced strong salinity stratification during the active phase, appears to inhibit heat transfer from the surface layer to greater depths.

Increased diurnal SST variation during the suppressed phase may relate to the relatively shallow surface mixed layer occurring over the phase. Aided by weak wind, strong salinity stratification, a small fraction of solar insolation penetrating the surface layer base, the shallow mixed layer, often shallower than 10 m during the day, distributes the total surface heat flux across a shallower depth and hence results in amplified diurnal SST variation during the suppressed phase.

Low-salinity water from Bay of Bengal and the Indonesian maritime continent likely explains the strong salinity stratification in the surface layer at the mooring site during suppressed phase when there is little precipitation. During the northwest monsoon season in December-March for example, when upper layer salinity in the Bay of Bengal is at its lowest, wind-driven currents advect low salinity water toward the mooring site. During July-September on the other hand, southeasterly winds associated with the southeast monsoon prevail and drive low salinity water from the maritime continent to the equatorial region.

Enhanced diurnal SST variations are a typical feature during the suppressed phase of the Kelvin waves across the tropical Indian Ocean. In the central equatorial Indian Ocean, the mean model δSST_d in response to the suppressed phase of a Kelvin wave during 15–19 November 2011 ranged between 0.2 and 0.6 °C (Baranowski et al., 2016; Seo et al., 2014). This range of values is comparable to the average δSST_d observed at our station, around 0.5 °C, over the course of the same Kelvin wave.

Our measurements reveal a significant correlation between diurnal SST variation and mean SST during the suppressed phase of the Kelvin waves. A similar relationship holds in the central Indian Ocean prior to the onset of the MJO convective phase (Seo et al., 2014). Using a set of numerical experiments, Seo et al. (2014) posited that diurnal SST raised time-mean SST and consequently latent heat flux into the atmosphere, which thereby moistened the lower troposphere, a favorable precondition for the MJO initiation. They further suggested that resolving diurnal SST variation, which has been underrepresented in the majority of general circulation models, would improve the MJO predictability. Given the coupled Kelvin wave—MJO nature in the Indian Ocean, determining whether diurnal SST variation during the suppressed phase affects the initiation of the Kelvin wave's convective phase would improve our understanding of the Kelvin wave as well as the MJO, but it requires moist static energy budget analysis that is beyond the scope of the present study.

The cumulative effect through the suppressed and active phases, or a full cycle, of the 15 Kelvin waves observed at the 0°, 90°E mooring on SST was a decrease in the order of 0.1 °C, and it is consistent with that derived from a larger number of Kelvin wave events across the tropical Indian Ocean between January 1998 to December 2012 as reported in a study by Baranowski et al. (2016). Despite acknowledging a persistent SST drop even after the passage of the Kelvin waves, Baranowski et al. (2016) attributed the SST drop to solely air-sea heat exchanges. In contrast, our results suggest that air-sea interactions, subsurface turbulence, and advection to a lesser extent dictate the SST cooling. We argue that sustained subsurface turbulence continues to cool SST past the active phase of the Kelvin waves, even after solar insolation begins increasing to warm the surface.

Observations of prolonged turbulent cooling across the surface mixed layer base in the wake of MJO wind events in the central equatorial Indian Ocean have been recently discussed in the literature (Moum et al.,

2016; Pujiana et al., 2018, 2015). SST cooling due to the MJO across the tropical Indian Ocean ranges between −0.3 and −1.1 °C (Chi et al., 2014; Moum et al., 2014; Pujiana et al., 2018). More energetic and longer duration wind stress variations may account for the larger SST drop during the MJO than we observe for convectively coupled Kelvin waves.

Moored temperature, salinity, and mixing measurements at select depths in the upper 60 m on the mooring allow an assessment of the time evolution of the barrier layer under the Kelvin wave convective systems. The observations illustrated that although the average BLT during the active phase was thicker than that during the suppressed phase by a factor of 2, the average rate of turbulent cooling near the base of the surface layer during the active phase was 3 times as large as that during the suppressed phase. Increased turbulent cooling across the base of the surface layer might relate to the fact that we measure turbulence at only two depths and have defined the surface layer as having a fixed depth coincident with the depth of our shallowest turbulence sensor. The mixed layer and ILD vary with time relative to the depths of our turbulence measurements, so we cannot resolve the actual turbulence evolution across the base of the vertically migrating mixed layer in relation to the variable thickness barrier layer. Employing indirect estimates of entrainment cooling, Drushka et al. (2014), Chi et al. (2014), and Horii et al. (2016) argued that entrainment of colder thermocline water into the surface mixed layer in the central and eastern equatorial Indian Ocean was minimum when the barrier layer was thick. Understanding these differences requires further investigation.

Acknowledgments
We acknowledge NOAA and its partners for maintaining the RAMA moored buoy array and for providing the opportunity to deploy χpod sensors (provided by Jim Moum of Oregon State University and funded by the National Science Foundation grant 1059055) on the 0°, 90°E mooring. The RAMA buoy data can be accessed at https://www.pmel.noaa.gov/tao/drupal/disdel/. This research was performed while the first author held a National Research Council Research Associateship Award at NOAA/PMEL. M. J. M. is supported by NOAA. This is PMEL contribution 4738.

References

Baranowski, D. B., Flatau, M. K., Flatau, P. J., & Matthews, A. J. (2016). Impact of atmospheric convectively coupled equatorial Kelvin waves on upper ocean variability. *Journal of Geophysical Research: Atmospheres*, *121*, 2045–2059. https://doi.org/10.1002/2015JD024150

Bentamy, A., & Fillon, D. C. (2012). Gridded surface wind fields from Metop/ASCAT measurements. *International Journal of Remote Sensing*, *33*(6), 1729–1754.

Chi, N. H., Lien, R. C., D'Asaro, E. A., & Ma, B. B. (2014). The surface mixed layer heat budget from mooring observations in the central Indian Ocean during Madden–Julian oscillation events. *Journal of Geophysical Research: Oceans*, *119*, 4638–4652. https://doi.org/10.1002/2014JC010192

Donlon, C. J., Casey, K. S., Robinson, I. S., Gentemann, C. L., Reynolds, R. W., Barton, I., et al. (2009). The GODAE high-resolution sea surface temperature pilot project. *Oceanography*, *22*(3), 34–45.

Drushka, K., Sprintall, J., & Gille, S. T. (2014). Subseasonal variations in salinity and barrier-layer thickness in the eastern equatorial Indian Ocean. *Journal of Geophysical Research: Oceans*, *119*, 805–823. https://doi.org/10.1002/2013JC009422

Fairall, C. W., Bradley, E. F., Hare, J. E., Grachev, A. A., & Edson, J. B. (2003). Bulk parameterization of air-sea fluxes: Updates and verification for the COARE algorithm. *Journal of Climate*, *16*(4), 571–591.

Horii, T., Ueki, I., Ando, K., Hasegawa, T., Mizuno, K., & Seiki, A. (2016). Impact of intraseasonal salinity variations on sea surface temperature in the eastern equatorial Indian Ocean. *Journal of Oceanography*, *72*(2), 313–326.

Kang, I. S., Liu, F., Ahn, M. S., Yang, Y. M., & Wang, B. (2013). The role of SST structure in convectively coupled Kelvin-Rossby waves and its implications for MJO formation. *Journal of Climate*, *26*(16), 5915–5930. https://doi.org/10.1175/Jcli-D-12-003031

Kiladis, G. N., Wheeler, M. C., Haertel, P. T., Straub, K. H., & Roundy, P. E. (2009). Convectively coupled equatorial waves. *Reviews of Geophysics*, *47*, RG2003. https://doi.org/10.1029/2008rg000266

Liebmann, B., & Smith, C. A. (1996). Description of a complete (interpolated) outgoing longwave radiation dataset. *Bulletin of the American Meteorological Society*, *77*(6), 1275–1277.

McPhaden, M. J., Meyers, G., Ando, K., Masumoto, Y., Murty, V. S. N., Ravichandran, M., et al. (2009). RAMA: The research moored array for African-Asian-Australian monsoon analysis and prediction. *Bulletin of the American Meteorological Society*, *90*(4), 459–000.

Moum, J. N., de Szoeke, S. P., Smyth, W. D., Edson, J. B., DeWitt, H. L., Moulin, A. J., et al. (2014). Air-sea interactions from westerly wind bursts during the November 2011 MJO in the Indian Ocean. *Bulletin of the American Meteorological Society*, *95*(8), 1185–1199.

Moum, J. N., & Nash, J. D. (2009). Mixing measurements on an equatorial ocean mooring. *Journal of Atmospheric and Oceanic Technology*, *26*(2), 317–336.

Moum, J. N., Pujiana, K., Lien, R. C., & Smyth, W. D. (2016). Ocean feedback to pulses of the Madden-Julian oscillation in the equatorial Indian Ocean. *Nature Communications*, *7*, 13203.

Nagura, M., & McPhaden, M. J. (2010). Dynamics of zonal current variations associated with the Indian Ocean dipole. *Journal of Geophysical Research*, *115*, C11026. https://doi.org/10.1029/2010JC006423

Osborn, T. R. (1980). Estimates of the local-rate of vertical diffusion from dissipation measurements. *Journal of Physical Oceanography*, *10*(1), 83–89.

Pujiana, K., Moum, J. N., & Smyth, W. D. (2018). The role of turbulence in redistributing upper-ocean heat, freshwater, and momentum in response to the MJO in the equatorial Indian Ocean. *Journal of Physical Oceanography*, *48*(1), 197–220.

Pujiana, K., Moum, J. N., Smyth, W. D., & Warner, S. J. (2015). Distinguishing ichthyogenic turbulence from geophysical turbulence. *Journal of Geophysical Research: Oceans*, *120*, 3792–3804. https://doi.org/10.1002/2014JC010659

Ridout, J. A., & Flatau, M. K. (2011). Convectively coupled Kelvin wave propagation past Sumatra: A June case and corresponding composite analysis. *Journal of Geophysical Research*, *116*, D07106. https://doi.org/10.1029/2010JD014981

Roundy, P. E. (2008). Analysis of convectively coupled Kelvin waves in the Indian Ocean MJO. *Journal of the Atmospheric Sciences*, *65*(4), 1342–1359. https://doi.org/10.1175/2007jas2345.1

Sengupta, D., Senan, R., Murty, V., & Fernando, V. (2004). A biweekly mode in the equatorial Indian Ocean. *Journal of Geophysical Research*, *109*, C10003. https://doi.org/10.1029/2004JC002329

Seo, K. H., Choi, J. H., & Han, S. D. (2012). Factors for the simulation of convectively coupled Kelvin waves. *Journal of Climate*, *25*(10), 3495–3514. https://doi.org/10.1175/Jcli-D-11-00060.1

Seo, H., Subramanian, A. C., Miller, A. J., & Cavanaugh, N. R. (2014). Coupled impacts of the diurnal cycle of sea surface temperature on the Madden–Julian oscillation. *Journal of Climate*, *27*(22), 8422–8443. https://doi.org/10.1175/jcli-d-14-00141.1

Straub, K. H., Kiladis, G. N., & Ciesielski, P. E. (2006). The role of equatorial waves in the onset of the South China Sea summer monsoon and the demise of El Niño during 1998. *Dynamics of Atmospheres and Oceans*, *42*(1-4), 216–238. https://doi.org/10.1016/j.dynatmoce.2006.02.005

Ventrice, M. J., Thorncroft, C. D., & Schreck, C. J. (2012). Impacts of convectively coupled Kelvin waves on environmental conditions for Atlantic tropical cyclogenesis. *Monthly Weather Review*, *140*(7), 2198–2214. https://doi.org/10.1175/Mwr-D-11-00305.1

Wang, Y., & McPhaden, M. J. (2017). Seasonal cycle of cross-equatorial flow in the central Indian Ocean. *Journal of Geophysical Research: Oceans*, *122*, 3817–3827. https://doi.org/10.1002/2016JC012537

Wheeler, M. C., & Hendon, H. H. (2004). An all-season real-time multivariate MJO index: Development of an index for monitoring and prediction. *Monthly Weather Review*, *132*(8), 1917–1932.

Wheeler, M., & Kiladis, G. N. (1999). Convectively coupled equatorial waves: Analysis of clouds and temperature in the wavenumber–frequency domain. *Journal of the Atmospheric Sciences*, *56*(3), 374–399.

Wheeler, M. C., & McBride, J. L. (2005). Australian-Indonesian monsoon. In W. K. M. Lau & D. E. Waliser (Eds.), *Intraseasonal variability in the atmosphere-ocean climate system* (pp. 125–173). Berlin: Springer.